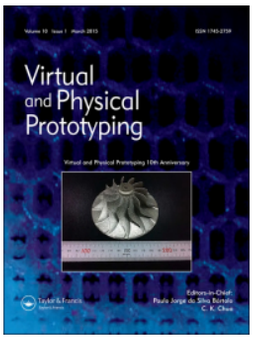

Taylor & Francis
Taylor & Francis Group

Virtual and Physical Prototyping

ISSN: 1745-2759 (Print) 1745-2767 (Online) Journal homepage: www.tandfonline.com/journals/nvpp20

Machine learning-based printability assessment and process control of aerosol jet 2D and 3D Printed PEDOT:PSS-based microstructures

Mohit Sharma & Miriam Seiti

To cite this article: Mohit Sharma & Miriam Seiti (2025) Machine learning-based printability assessment and process control of aerosol jet 2D and 3D Printed PEDOT:PSS-based microstructures, Virtual and Physical Prototyping, 20:1, e2575397, DOI: 10.1080/17452759.2025.2575397

To link to this article: https://doi.org/10.1080/17452759.2025.2575397

VIRTUAL AND PHYSICAL PROTOTYPING
2025, VOL. 20, NO. 1, e2575397 (19 pages)
https://doi.org/10.1080/17452759.2025.2575397

Taylor & Francis
Taylor & Francis Group

Machine learning-based printability assessment and process control of aerosol jet 2D and 3D Printed PEDOT:PSS-based microstructures

Mohit Sharma [a]* and Miriam Seiti [b,c]*

[a]Department of Electrical Engineering (ESAT), STADIUS Center for Dynamical Systems, Signal Processing and Data Analytics, KU Leuven, Leuven, Belgium; [b]Department of Mechanical and Industrial Engineering, University of Brescia, Brescia, Italy; [c]Department of Mechanical Engineering, Campus De Nayer, KU Leuven, Sint Katelijne-Waver, Belgium

ABSTRACT

Aerosol Jet Printing (AJP) is a high-resolution additive manufacturing technique applied for two-dimensional (2D) and three-dimensional (3D) microstructures. Typical inks refer to metal solutions, but also conductive polymers, such as poly(3,4-ethylenedioxythiophene):polystyrene sulfonate (PEDOT:PSS), have been widely printed by AJP. However, optimising the AJP process remains challenging due to the non-linear, geometry-dependent effects of parameters including carrier gas flow, sheath gas flow, and platen temperature. This study introduces a physics-informed machine learning (ML) framework for predicting print quality and selecting process parameters. To our knowledge, this is the first unified, data-driven comparison of 2D lines and 3D high-aspect-ratio (HAR) pillars with PEDOT:PSS inks, revealing how process physics shift from single-layer deposition to layer-by-layer growth. Datasets were expanded with virtual sample generation and physics-based feature engineering. Five ML models, namely Random Forest, Gaussian Process Regression, Support Vector Machines, Generalised Additive Models, and Neural Networks, were trained and tuned with nested cross-validation and Bayesian optimisation. The best-performing models achieved high predictive accuracy ($R^2 > 0.9$ for 2D; $R^2 \approx 0.7$ for 3D). The framework shows that 3D AJP operates within a significantly narrower process window, with carrier gas flow requiring more than four times tighter control than in 2D AJP.

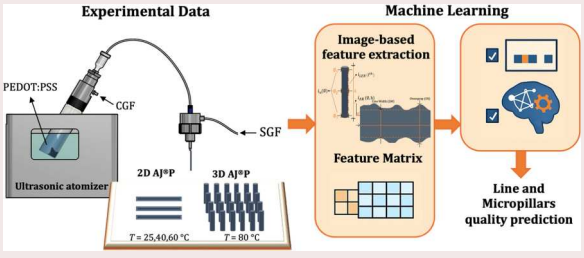

ARTICLE HISTORY
Received 22 July 2025
Accepted 9 October 2025

KEYWORDS
Machine learning; aerosol jet printing; predictive modelling; process optimization; PEDOT:PSS

1. Introduction

Printed Electronics (PE) is an emerging field which exploits Additive Manufacturing (AM) technologies for the design, development and production of passive and active electronic elements [1]. The main technologies used in PE include screen printing, roll-to-roll printing, inkjet printing (IJP), and aerosol jet printing (AJP), each offering distinct advantages in terms of resolution, throughput, substrate compatibility, and ink versatility [2,3]. For instance, screen printing is widely adopted for its scalable and high deposition thickness, particularly useful in the fabrication of conductive traces on large-area substrates [4]. Roll-to-roll printing enables continuous, high-speed production on flexible substrates, making it ideal for industrial-scale manufacturing [5]. IJP provides digital, maskless, planar patterning, suitable for rapid prototyping and low-volume production [6]. Alternatively, AJP offers its high-resolution capabilities down to 10 µm in linewidth and 100 nm in layer thickness [7]. Compared to the other technologies, AJP is a non-contact, maskless AM technique

CONTACT Miriam Seiti miriam.seiti@unibs.it University of Brescia, Department of Mechanical and Industrial Engineering, Via Branze 38, 25123, Brescia, Italy.
*Both authors contributed equally.
Supplemental data for this article can be accessed online at https://doi.org/10.1080/17452759.2025.2575397.
In Supplementary Information, Table 1 please add reference [24]
In Supplementary Information, Table 2 please add reference [21]

capable of printing fine features on *free-form* substrates, including 3D and non-planar surfaces. AJP typically uses functional nanoinks with a wide range of viscosity (1-100 mPas) and a particle size $\leq$ 0.5 µm [8]. This ability to process a wide range of inks, from metal nanoparticle (NPs) suspensions, polymers, to biological materials, makes it particularly attractive for advanced use cases in microelectronics, biomedical devices, and complex multi-layer architectures [9,10,11]. AJP planar structures are commonly used in sensors, antennas, interconnects, and thin-film electronics, where accurate, high-resolution deposition on flat or curved surfaces is critical [12]. Beyond the fabrication of conventional two-dimensional (2D) patterns, AJP, unlike IJP, has also been recently applied for the building up of three-dimensional (3D) microstructures with high aspect ratios (HAR), including micropillars, lattice structures, and interconnects [10,13,14,15]. These microstructures are used in microscale technologies to enhance electrical performance, increase surface area, and enable efficient thermal or charge transfer. They indeed typically find use in applications like microelectronics, energy storage, photonics, sensors, and also microfluidics [16,17]. Microstructures fabricated by 3D AJP have indeed explored in energy harvesting and sensing devices [18,19,20]. The successful fabrication of both 2D and 3D structures by AJP relies on fine tuning multiple process parameters, including carrier gas flow (*CGF*, *CGF* = [0–50] sccm) and sheath gas flow (*SGF*, *SGF* = [0–200] sccm), nozzle-substrate distance z = [0–5] mm, print speed s = [0–400] mm/sec, platen temperature *T* = [20–100] °C, and post-processing conditions, such as sintering temperature and time. However, the relationships between process parameters and functional outcomes are often highly nonlinear, interdependent, and especially geometry dependent [22]. This implies that the same process parameters must be adjusted when transitioning between 2D and 3D AJP, as using identical settings for both geometries typically fails and does not ensure satisfactory print quality. In addition, although its versatility and high resolution, AJP still faces challenges such as limited repeatability, sensitivity to process parameter variations, and difficulties in maintaining uniform print quality across different substrates and geometries. Consequently, manual parameter optimisation, whether by trial-and-error or design of experiments (DOE), remains the most used method to fine-tune the print settings. However, this approach is time-consuming and often insufficient for ensuring reliable print quality across different pattern types.

In recent years, ML approaches have gained attention to accelerate process optimisation in AM by enabling data-driven modelling of complex input – output relationships. In the context of AJP, ML has been applied to predict isolated features such as linewidth or film resistance, primarily for 2D structures. For instance, Li et al. [23] proposed a ML workflow that combines image-based feature extraction using convolutional neural networks (CNNs) with regression models, such as support vector regression, random forest, and Gaussian process regression, to predict the electrical resistivity of 2D AJP lines based on process parameters (*CGF*, *SGF*, *s*) and printed morphology to predict electrical resistivity, achieving high prediction accuracy with R^2 values up to ≈0.92. Also Liu et al. [34]. applied a ML framework that, using support vector machines and Gaussian process regression, linked droplet morphology and process parameters (*CGF*, *SGF*, *s*) to printed line characteristics. Differently, Zhang et al. [23] developed a ML framework integrating K-means clustering, support vector machine (SVM) classification, and Gaussian process regression to predict droplet diameter and thickness in AJP, enabling process optimisation across a five-dimensional parameter space (*SGF*, *CGF*, *s*, *z*, and *T*), with root mean square errors as low as 1.84 µm for diameter and 0.11 µm for thickness. In addition, Zhang et al. developed an integrated ML approach for autonomous tuning of AJP process parameters with CNNs and in-situ anomaly detection. The system achieved and R^2 of ∼ 0.89, accuracies of 95.3% for process optimisation and 92.7% for anomaly detection, demonstrating the effectiveness of the proposed method in enabling robust control and fault detection during printing.

However, limited attention has been devoted to developing ML frameworks capable of supporting both 2D and 3D geometries, enabling predictive modelling and optimisation across diverse structure types. Such a framework would enable more efficient parameter tuning, reduce experimental effort, and enhance the transferability of process insights across different structural designs.

Therefore, this study introduces a physics-informed ML framework for predicting and optimising print quality in the AJP of both 2D lines and 3D HAR microstructures. Building on our previous works based on DOE approaches applied for optimising 2D and 3D AJP of printed lines and HAR microstructures, respectively [22,25], this manuscript consolidates and expands the datasets into a robust ML framework that, for the first time, addresses the AJP of the conductive polymer Poly(3,4-ethylenedioxy thiophene)polystyrene sulfonate (PEDOT:PSS) across both geometries. The process window was systematically explored by mainly varying *CGF*, *SGF* and *T*, identified as the primary parameters influencing print quality. Importantly, this work provides the first unified, data-driven analysis of PEDOT:PSS printed by AJP, revealing how process physics evolve from single-layer 2D line deposition to layer-by-layer 3D microstructure fabrication.

These parameters were explored across their full process windows, and the resulting experimental data

were used to train supervised ML models aimed at optimising printability. PEDOT:PSS was selected as the functional material due to its widespread use in PE, attributed to its high electrical conductivity, flexibility, and processability [26]. Particularly, in this study two PEDOT:PSS-based inks were used: one commercial solution optimised for 2D AJP and one tailored for 3D AJP. The latter required the addition of specific rheology-modifying additives to enable the build-up of HAR, otherwise, the ink would only produce planar 2D features.

To systematically investigate the distinct process-quality relationships associated with each geometry, this study implements a multi-stage learning pipeline separately to the 2D and 3D datasets. The objective is to move beyond traditional DOE approaches and exploit predictive modelling to extract deeper insights and optimal parameter windows for 2D and 3D AJP. The framework begins with physics-informed feature engineering and data augmentation using the Synthetic Minority Oversampling Technique for Regression (SMOTE-R), which addresses the practical limitations imposed by the scarcity of experimental data. A diverse set of five supervised learning models is rigorously trained and tuned using Bayesian optimisation within a nested cross-validation architecture. This ensures robust model performance while preventing data leakage and overfitting. The predictive accuracy is further enhanced by combining these models into a stacked ensemble, with ridge regression serving as 'meta-learner'. The tuned models for each geometry are then deployed as computationally efficient surrogate functions within constrained optimisation framework to identify the optimal process windows. This comprehensive, data driven methodology allows a direct assessment of geometry-specific process sensitivities. Moreover, it offers a validated framework for AJP optimisation, building meaningfully on the insights gained through earlier DOE approaches [22,25]. Therefore, this manuscript proposes a physics-informed ML framework to study previously unavailable AJP process insights on the printing of PEDOT:PSS by systematically comparing 2D lines and 3D HAR pillars. Main results show that 2D print quality is primarily caused by jet collimation, whereas 3D pillar quality is dominated by material deposition rate (*CGF*) within a tighter process window. The analysis quantifies more than four times tighter *CGF* tolerance for 3D than for 2D, explaining the greater susceptibility of 3D AJP to parameter change.

2. Materials and methods

2.1. Materials

PEDOT:PSS-based formulations were selected as AJ®P material. For 2D AJ®P, a commercial PEDOT:PSS ORGACON™ Transparent Conductive Ink IJ-1005 (AGFA NV, BE) was used. This ink is a water-based dispersion containing 0.8 wt% of PEDOT:PSS and 12–20 wt% diethylene glycol (DEG) as a co-solvent. The main ink properties are: viscosity $\eta = [7–12]$ mPa·s, surface tension s = [31-34] mN/m, and surface resistance $r \sim 800\ \Omega$/sq. An own formulated PEDOT:PSS was instead employed for 3D AJP. As previously mentioned, the ink intended for 3D AJP, was modified from standard 2D formulations by incorporating specific co-solvents and additives. These adjustments enable the formation of microstructures by ensuring a fast evaporation rate of the solvent system during in-flight jetting, along with a solid content sufficient to support the buildup of 3D features. The ink for 3D AJP was prepared starting from a water-based dispersion of PEDOT:PSS at 1.3 wt% (Sigma Aldrich 483095, BE), with the addition of 1–5 wt % polyethylene glycol (PEG, Mw = 400 Da), 1–5 wt% carboxymethyl cellulose (CMC), 5–10 wt% ethylene glycol (EG). The ink exhibits a viscosity $\eta = [3–7]$ mPa·s, a surface tension of $\gamma \sim 72$ mN/m, and a conductivity $\sigma = 495.29$ S cm^{-1}. Glass slides (Superfrost, VWR, BE) were used as substrates.

2.2. Methods

2.2.1. 2D and 3D AJP processes

Printed samples were obtained in previous works using an Optomec AJ®P 300s system (Optomec®, USA) equipped with the ultrasonic atomiser configuration (Figure 1(a)). The protocols followed are described in detail in Seiti et al. [25] and Ceretti et al. [22] Briefly, both PEDOT:PSS inks were sonicated for 10 min at 25 °C, and aerosolized in the glass vial with a power atomisation voltage of 48.5 V at a volume of ~850 µL. The aerosolized ink was transported to the deposition head by the *CGF* and aerodynamically focused by the *SGF* to form a stable aerosol jet, which was subsequently ejected from the nozzle and deposited onto the selected substrate. Nitrogen (N_2) served as both *CGF* and *SGF*. The 2D AJP design consisted of a single line 1 cm in length with an approximate width of 150 µm. For 3D AJP, arrays of 6×4 micropillars were instead printed, each with a diameter of 50 µm and a center-to-center spacing of 150 µm. Each condition analysed had at least three replicas. Following printing, the printed samples were thermally cured in a Heraeus oven at 140 °C for 1 h.

Table 1 reports the main print parameters used for 2D and 3D AJP. All experiments were performed under ambient conditions (22 °C, 55% rh). For both 2D and 3D AJP processes, the two key parameters, that is *CGF* and *SGF* were analysed using DOE approaches. The

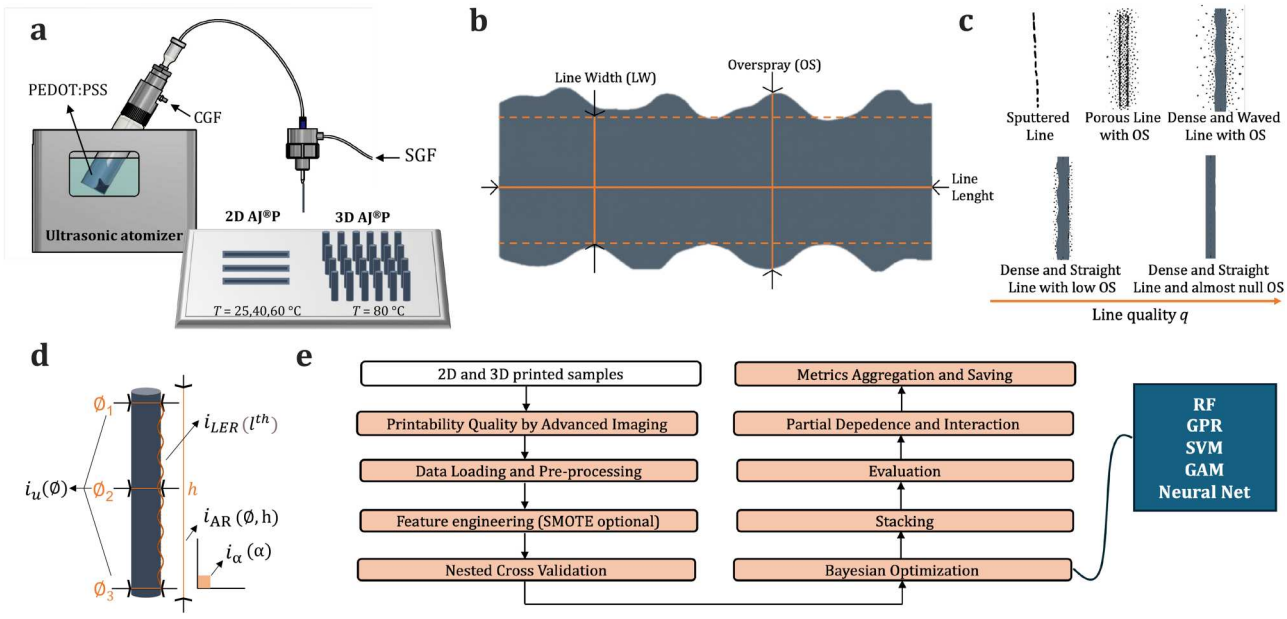

Figure 1. Process methodology: (a) AJP working process for 2D and 3D AJP, Modified with permission from Seiti et al. [21]. Copyright Elsevier, 2022. (b) 2D AJP line detection, (c) 2D AJP line quality q ranking, (d) 3D AJP printability and shape fidelity sub-indexes. Reproduced from Ceretti et al. [22] with permissions from Elsevier 2025, (e) ML workflow for 2D and 3D AJP.

Table 1. Process parameters for 2D and 3D AJ®P of PEDOT:PSS-based formulations [22,25].

2D AJP process parameters							
Factors	Levels						
Carrier gas flow, *CGF* [sccm]	10	20	30	40		50	
Focusing Ratio, *Rf* [#]	1-1.5-2	1-1.5-2	1-1.5-2	1-1.5-2		1-1.5-2	
Platen temperature, *T* [°C]	25		40		60		
General Response	Print quality index *q*						
3D AJP process parameters							
Factors	**Levels**						
CGF [sccm]	20	22.5	25	30	35	40	45
Rf [#]	1-1.2-1.4-1.6-2-3-4	1.2-1.4-1.6	1-1.2-1.4-1.6-2-3-4	1-2-3-4	1-2-3-4	1-2-3-4	1-2-3-4
T [°C]	80						
General Response	Printability and Shape Fidelity Index, Ψ [#]						
Fixed Parameters	**2D AJP**			**3D AJP**			
Sample design	Printed line of 10 mm			Array of 6 × 4 circles, Ø = 50 µm			
Nozzle diameter, Ø [µm]	300			150			
Print speed, *s* [mm/sec]	25			0.4			
Number of layers, *n* [#]	10			25			
Substrate	Glass slides, VWR Superfrost® Plus Micro Slide						
Stand-off distance, *z* [mm]	3						

interactions between *CGF* and *SGF* were investigated because the *Rf*, defined as the ratio of *SGF* to *CGF*, is a key parameter in AJ®P for achieving high resolution patterns, thus high-quality printing. For a given nozzle diameter, *Rf* influences the aerosol beam's shape, size, and particle distribution. Therefore, a convergent $Rf \geq 1$ is essential to produce a well-focused mist and minimise overspray (OS) (*i.e.* satellite droplets along the printed pattern edges) caused by off-trajectory droplets.

For 2D AJP, the DOE included *Rf* values of (1, 1.5, 2), each combined with five specific *SGF* – *CGF* combinations. Platen temperature was also varied across three levels: $T = (25, 40, 60\,°C)$. For 3D AJP, the DOE covered a window with $Rf = (1, 2, 3, 4)$ and $CGF = (20, 25, 30, 35, 40, 45)$ sccm, along with a refined sub-window of $Rf = (1.2, 1.4, 1.6)$ and $CGF = (20, 22.5, 25)$ sccm. A single platen temperature of $T = 80\,°C$ was used in 3D AJP, as lower temperatures were previously

shown to prevent microstructure formation. The response of interest was the quality of the printed patterns, as detailed in Section 1.2.2. Optical images of printed samples were acquired using a digital microscope (Hirox KH8700, CZ) and analysed with ImageJ software.

2.2.2. 2D and 3D printability indexes

Print quality is here defined as the ability of the printing process to consistently reproduce patterns that closely match the proposed design in terms of shape accuracy, fidelity, and repeatability. Two printability indexes (PIs) were developed for 2D and 3D AJP by integrating optical and analytical methods to directly correlate process parameters with geometric outcomes. For 2D AJP, the PI focused on visual quality of the printed line. An ideal line is characterised as a dense, well-defined track with straight edges and minimal OS (Figure 1(b)). As shown in Figure 1(c), line quality index, defined as q_{2D}, was evaluated using an ordinal ranking system ranging from poor to optimal. The categories included: (a) sputtered lines; (b) porous lines with pronounced OS; (c) low-density, irregular lines with OS; (d) dense yet wavy lines with OS; and (e) dense, well-defined lines with minimal OS [25]. The microstructure quality index for 3D AJP, here referred as q_{3D}, was established in prior work [22], considering the arithmetic mean of four sub-indexes that quantify key geometric features of HAR micropillars, as illustrated in Figure 1(d). These sub-indexes include: (i) uniformity index (i_u) [#], (ii) aspect ratio index (i_{AR}) [#], (iii) bending angle index (i_α) [#], and (iv) line edge roughness index (i_{LER}) [#]. Each PI (and sub-index) is expressed as a continuous variable ranging from 0 to 1, where 0 represents the ideal geometry, a perfect line for 2D patterns or a cylinder for 3D structures.

2.3. Machine learning framework for printability optimisation

An overview of ML framework employed in this study to model and optimise the print quality in AJP is presented in Figure 1(e). This section details the key components of the methodology, including data preprocessing, representation of domain knowledge through physics-informed features, data augmentation, and the proposed ML pipeline for predictive modelling and optimisation.

2.3.1. Data preprocessing and representation

The structure and preparation of the experimental data, including normalisation of target variables, derivation of physically meaningful features, and incorporation of domain constraints to inform the learning process, is prepared.

2.3.2. Dataset composition and inclusion of physical constraints

The experimental dataset consists of 171 samples from 2D line printing and 63 from 3D micropillar fabrication (including repetitions), as summarised in Table 1. To improve model generalizability and embed domain constraints, the dataset was augmented with a binary indicator for parameter combinations where the *SGF* is lower than the *CGF*. These conditions correspond to a $Rf < 1$, which is widely recognised in the literature to produce unstable, divergent aerosol jets and consistently poor print quality [27]. These undesirable regions in the process parameter space were annotated with a binary indicator labelled InvalidFocus.

This augmentation strategy introduces domain knowledge into the learning process, ensuring that the models are explicitly aware of non-viable regions within the process parameter space. As a result, it acts as a safeguard against the generation of undesirable or unprintable process conditions during optimisation, improving the reliability and physical validity of the predicted optimal parameters.

2.3.3. Normalisation of the prediction target

To ensure consistency across datasets and enable robust comparative analysis, both PIs described in Section 2.2.2 were transformed into a single, normalised quality score bounded between 0 and 1.

For the 3D AJP dataset, the printability index defined in Ceretti et al. [22] was inverted to establish a 'higher-is-better' quality measure, using the transformation:

$$q^*_{3D} = 1 - q_{3D} \tag{1}$$

For the 2D AJP dataset, the original index from Seiti et al. [25] was linearly rescaled using:

$$q^*_{2D} = \frac{q_{2D} - 1}{\max(q_{2D}) - 1} \tag{2}$$

where, q_{2D} and q_{3D} is the original printability score for 2D and 3D AJP.

This normalisation step ensures that both transformed target variables operate on a consistent [0, 1] scale, where 1 corresponds to the ideal print quality and 0 signifies the worst.

2.3.4. Derivation of physically informed predictors

To enhance the predictive performance of the ML models and ensure alignment with the physical principles governing AJP, three additional predictors were derived from the primary process variables *CGF* and

SGF: the total gas flow (*TGF*), the logarithm of *Rf*, and the invalid *Rf* flag. The *TGF* is defined as the sum of *CGF* and *SGF*, serves as an indicator of the total volumetric gas throughput within the printhead. It correlates with the kinetic energy of the aerosol stream, influencing the material delivery rate and feature resolution during printing [28]. The logarithm of *Rf* considers the *Rf*, which is the critical dimensionless quantity governing aerosol stream collimation [29]. Given its nonlinear relationship with printing outcomes, [27,30] a logarithmic transformation was applied:

$$Log - FocusRatio = \log(Rf) \triangleq \log\left(\frac{SGF}{CGF}\right) \quad (3)$$

This transformation improves linearity in the predictor-response relationship.

Finally, the invalid *Rf* flag is a binary variable was introduced to flag parameter combinations where $SGF < CGF$ (*i.e.*, $Rf < 1$), which consistently leads to defocused jets and printing failure [27]. This variable acts as a physically informed penalty that discourages the model from recommending unprintable parameter regimes.

2.3.5. Data augmentation: virtual sample generation (VSG)

A persistent challenge in deploying ML for manufacturing process optimisation is the limited availability of high-quality experimental data due to the significant time investment associated with each experimental run to cover the complete continuous process window available [31]. This scarcity is particularly problematic when modelling optimal or near-optimal process windows, which are typically underrepresented in the data due to the constraints of traditional experimental design [31,32].

To address this limitation, we adopted the Synthetic Minority Over-sampling Technique for Regression (SMOTE-R) is adopted [33]. In contrast to its classification counterpart [34], SMOTE-R generates synthetic samples through interpolation between existing data points in the feature space, with a focus on underrepresented regions enriching underrepresented regions of the dataset [33,35]. In the present context, this allowed targeted augmentation of the high-quality printability regime, which is of practical interest.

An augmentation ratio of 100% (a 1:1 real-to-synthetic ratio) was selected as a conservative setting, generating augmented training set for the 2D AJP (Figure 2(a)) and the 3D AJP (Figure 2(b)). This setting increased local sample density in sparse, high-performing regions of the process window while preventing synthetic data from dominating the training signal. To ensure the fidelity and physical validit, three critical safeguards were implemented. First, data synthesis was performed exclusively within the training set of each inner fold of the nested cross-validation pipeline. This prevented any leakage of synthetic information and preserved unbiased estimates of generalisation performance. Second, the generation of synthetic samples was constrained by process physics, specifically, the condition that $SGF \geq CGF$ was used and the values of *T* were restricted to the levels specified in the experimental design. Derived features, such as the Log-FocusRatio and Total Gas Flow, were recalculated for each synthetic point to maintain internal consistency.

Finally, the validity of the augmented data was evaluated through a formal statistical comparison of the synthetic and original datasets. This validation involved two quantitative measures, *i.e.* the two-sample Kolmogorov–Smirnov (KS) test and the Maximum Mean Discrepancy (MMD), shown in Supplementary Figure 3. This was complemented with visual inspection of overlaid probability density functions (PDFs) for each primary predictor and the quality index.

2.4. ML based predicitve modelling

The ML pipeline was architected to ensure robust model training, unbiased hyperparameter tuning and unbiased evaluation of model performance, as described in the following sections.

2.4.1. Regression models

To effectively capture the physical interactions underlying AJP, a diverse suite of five supervised regression algorithms was selected to serve as base learners with different learning strategies (*e.g.* ensemble, probabilistic, kernel-based, additive) [46,47]. The algorithms chosen are: (i) Tree-based learners (RF), which excel in capturing discrete operational thresholds and are preferred for tabular data with structured feature; (ii) Kernel methods (SVM, GPR) which handle smooth nonlinear manifolds and, in the case of GPR, enable the capability of providing reliable prediction variance when dealing with limited or incomplete data; (iii) Additive models (GAM) learn non-linear relationships by fitting smooth, non-parametric functions to individual features and summing their effects, offering a balance between flexibility and interpretability; and (iv) Neural networks (NN), capable of approximating arbitrary non-linear functions, including complex, latent interactions that may not be easily captured by traditional kernel or tree-based models. Table 2 provides a summary of the selected models, highlighting their respective relevance for

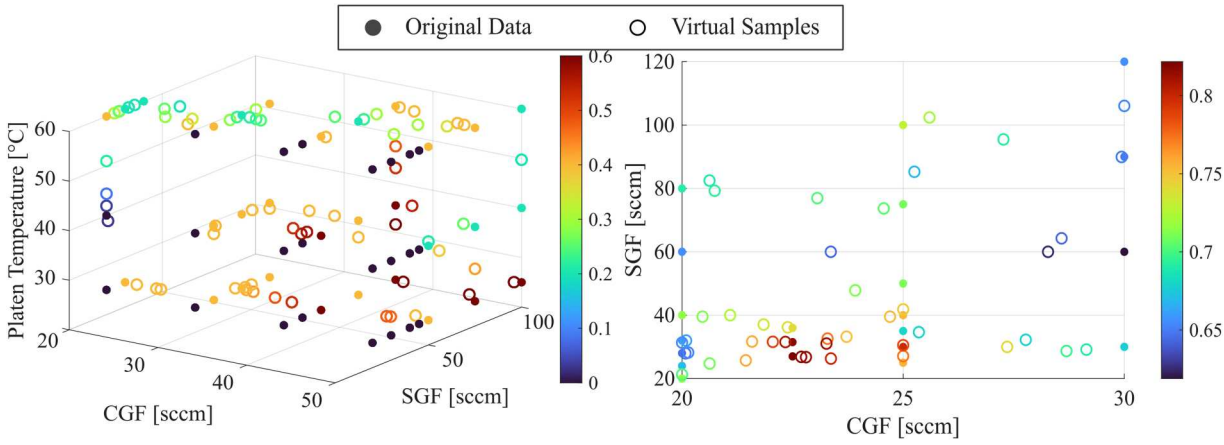

Figure 2. SMOTE-R based synthetic data augmentation in feature space: 3D scatter of original and synthetic data points for (a) 2D geometry, spanning all platen temperatures, (b) 3D geometry, shown only at a fixed platen temperature of 80 °C. Colors represents target quality variable.

Table 2. Overview of models selected for printability optimisation of AJ®P based microstructures.

Acronym	Model Type	Relevance to AJP Optimisation
RF	Random Forest *(Ensemble of Trees)*[36,37]	An ensemble method that captures high-order feature interactions. It is highly effective at capturing complex non-linear relationships and interactions between features and is inherently robust to outliers.
GPR	Gaussian Process Regression [38,39]	A non-parametric, Bayesian approach to regression that models the target variable as a Gaussian process. It is well suited for uncertainty quantification in small, potentially noisy datasets common in manufacturing.
SVM	Support Vector Machine *(Radial Basis Function (RBF) kernel)*[40,41]	A kernel-based model for regression that maximises generalisation margin and resists overfitting through a regularised loss. The RBF kernel accommodates complex nonlinearities in flow dynamics by projecting the data into a higher-dimensional feature space.
GAM	Generalised Additive Model *(Penalized Splines)*[42,43]	An interpretable model that enables interpretable learning through smooth univariate splines and selective interaction terms. It offers a balance between flexibility and the ability to understand the contribution of each feature to the prediction.
NN	Neural Network *(2 Hidden Layers)*[44]	A universal function approximators that can learn higher-order nonlinearities and latent interactions. Given the data size, shallow feed-forward neural network with only two hidden layers prevents overfitting.

sparse experimental data, and practical advantages for AJP optimisation.

2.4.2. Hyperparameter tuning: nested cross-validation and bayesian optimisation

To ensure robust model generalisation and to mitigate the risks of overfitting and data leakage, a rigorous nested cross-validation (nCV) framework was employed for both hyperparameter optimisation and performance evaluation. This methodology is critical for small-sample problems, where efficient utilisation of limited data must be balanced against the need for statistical validity.

Outer cross-validation loop

A 5-fold cross-validation was adopted to evaluate the generalisation performance of each model, while avoiding overfitting. In each of the five outer iterations, the data was split into an outer test fold (used for final validation) and an outer training set (comprising the remaining four folds). This outer training set was then passed to the inner loop for model training and hyperparameter optimisation. The final performance metrics represent the average prediction accuracy across the five outer test folds.

Inner model training and hyperparameter optimisation loop

Within each outer training set, a 2-fold cross-validation was employed to train and validate candidate models across a range of hyperparameter configurations. For each candidate hyperparameter configuration, the model was trained on one inner fold and validated on the other, with Root Mean Squared Error (RMSE) serving as the objective function. This process was

repeated across both inner folds, and the average RMSE was recorded.

To efficiently explore the high-dimensional hyperparameter space and avoid exhaustive grid search, the Bayesian optimisation is utilised. Unlike traditional grid search methods, Bayesian optimisation employs a surrogate model, typically a Gaussian Process, to approximate the relationship between a model's hyperparameters and the objective function. This surrogate model is continuously updated using Bayesian inference, as new evaluations are conducted. At each iteration, the updated surrogate model guides the selection of the next hyperparameter configuration by balancing exploration (searching unexplored regions) and exploitation (refining around promising areas). This iterative process allows Bayesian optimisation to efficiently converge toward an optimal set of hyperparameters using far fewer evaluations than exhaustive grid search. The optimisation was capped at 30 iterations per model, which balances the computational cost with sufficient exploration of the hyperparameter space.

This nested structure ensures that model training and hyperparameter tuning is completely isolated from the outer test fold, thus providing an unbiased and statistically valid estimate of model performance.

In addition to this primary evaluation framework, a supplementary targeted diagnostic analysis is performed for the NN model to clarify its training dynamics and generalisation behaviour. For each geometry, the NN was retrained on a single 80/20 training/validation split of the augmented dataset, using the architecture and hyperparameters tuned by Bayesian optimisation within the nested cross validation pipeline. The search spanned wide ranges for the two hidden layer widths and for the L2 regularisation coefficient λ, with λ in [10−6, 10−2].

Epoch-wise training and validation mean-squared errors (MSE) were recorded to generate learning curves (Supplementary Figure 1) and to assess potential overfitting or convergence issues. During the diagnostic training, dropout was active for the training set and inactive for the validation set. It is critical to note that this diagnostic analysis of the NN was performed solely for interpretation and did not affect model selection or hyperparameter tuning. All performance metrics reported in Section 3.2 derive exclusively from the nested cross-validation procedure.

3. Results

This section presents the empirical results of the ML-driven framework developed to predict and optimise print quality in AJP. The subsequent analysis extends beyond mere predictive accuracy to demonstrate how these models can be leveraged for process window identification and parameter optimisation, addressing key challenges in AM such as quality control, process repeatability, and the push towards zero-defect manufacturing [45].

3.1. Experimental 2D and 3D AJP results

For 2D AJP, the geometrical characteristics of the printed lines obtained at different values of *Rf*, *CGF* at the different platen temperatures, that is $T = 25$ °C, $T = 40$ °C and $T = 60$ °C, are presented in Figure 3(a–c), respectively. In each graph, both the line width (LW) and the total width including overspray (LW + OS) are reported. Figure 3(d) shows representative printed lines at $T = 40$ °C for each *Rf* (1, 1.5, 2) and *CGF* (20, 30, 40, 50 sccm) combination. These images confirm that higher *Rf* values result in narrower lines and therefore high-resolution patterns. Supplementary Table 1 reports the line width values ($\mu + \sigma$) for each combination. Additionally, higher *CGFs* generally lead to increased material deposition, causing wider lines. Generally, low *Rf* and low *CGF* values produces poor jet convergence, therefore low control in pattern definition. Figure 3(e and f) further illustrate the ability to print at high quality quality 2D patterns. Figure 3(e) shows a representative 2D printed pattern, demonstrating uniform line formation and minimal OS. Figure 3(f) presents a crosshatch pattern using the same parameters, confirming good directional consistency, jet stability, and overall process reliability under the selected conditions. Figure 4 and Figure 5 illustrate the effects of varying *CGF* and *Rf* conditions on the 3D AJP process. Supplementary Table 2 depicts the geometrical metrics (μ±σ) of each sub-index for the calculation of the printability quality index for any combination analysed. As discussed Ceretti et al. [22] not all tested parameter combinations resulted in the successful formation of micropillars. When using a $CGF \geq 35$ sccm, excessive material deposition prevented pillar formation, leading instead to large, coalesced structures (Figure 4). At *CGF* = 20 sccm, micropillar formation was observed, but with irregular morphology and some merging at the tips. A more stable and consistent micropillar geometry was achieved with *CGF* values between 25 and 30 sccm. Regarding the *Rf*, when *Rf* = 1, the pillars are well-defined, whereas at *Rf* = 3, increased surface roughness and bending are evident. As shown in Figure 5, within the optimised *CGF* range of 20–25 sccm more regular and vertically aligned micropillars are instead observed, demonstrating the stability within this process window.

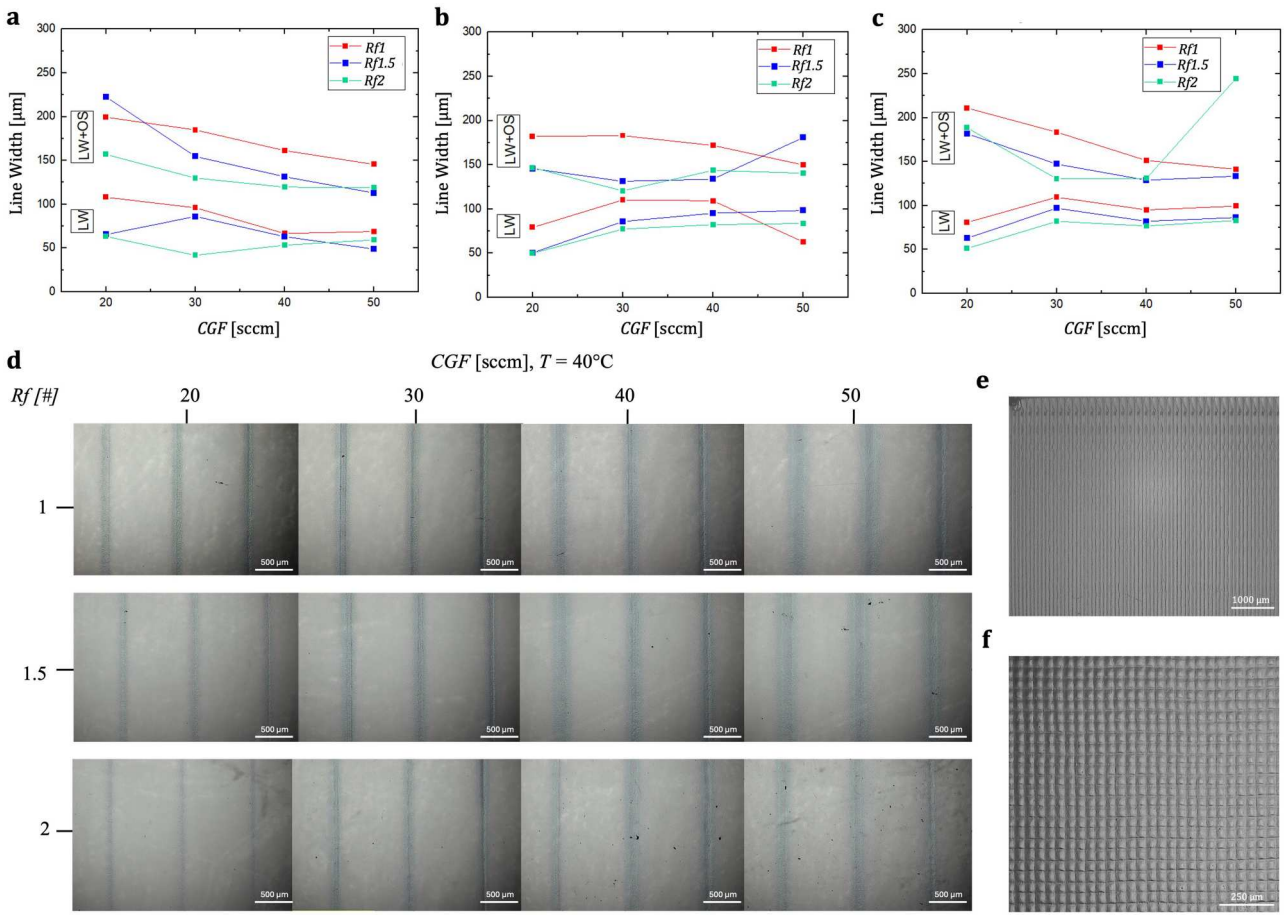

Figure 3. 2D AJ®P of PEDOT:PSS-based ink: Line width and overspray (OS) results for (a) $T = 25$ °C, (b) $T = 40$ °C, and (c) $T = 60$ °C; (d) Representative images of 2D printed lines at $T = 40$ °C for each combination of *Rf* and *CGF* analysed, (e) Representative image of a 2D printed pattern obtained under the best printing conditions, (f) Crosshatch pattern printed in both x and y directions using the same optimal parameters (N = 3). Raw data from [25].

3.2. Validation of synthetic data augmentation

The statistical validation demonstrates that the SMOTE-R augmented data accurately reproduce the distributions of the original experimental datasets while remaining consistent with all physical and experimental constraints. Quantitative results are provided in the Supplementary Information (Supplementary Figure 3).

For the 2D dataset, the distributions of the primary process parameters were well preserved. The gas flow distributions also showed strong alignment with the experimental data (*CGF*: $p = 0.042$, D = 0.298; *SGF*: $p = 0.078$, D = 0.273). While the KS test identified a statistically significant difference for the 2D quality index ($p = 0.001$), this is consistent with the sparse and multimodal nature of the quality distribution. Visual inspection of the overlaid probability density functions confirmed that the synthetic data preserved the location and relative prominence of the original peaks. This observation is further supported by a modest MMD^2 value of 0.186.

For the 3D dataset, the analysis shows strong distributional agreement across all variables, with no statistically significant differences detected (*CGF*: $p = 0.304$; *SGF*: $p = 0.797$; Quality index: $p = 0.154$). These results, combined with the methodological safeguards described in Section 2.3.5, provide robust evidence that the 100% augmentation strategy increased local data density without introducing out-of-manifold points or compromising the integrity of the training data.

3.3. Model performance evaluation

To assess the predictive accuracy and generalisation capability of the candidate ML models, a robust nested cross-validation framework was employed. This methodology ensures statistically unbiased performance estimates by isolating model evaluation from both training and hyperparameter optimisation, hence preventing data leakage and overly optimistic results.

Model performance was quantitatively evaluated using three widely adopted regression metrics: RMSE,

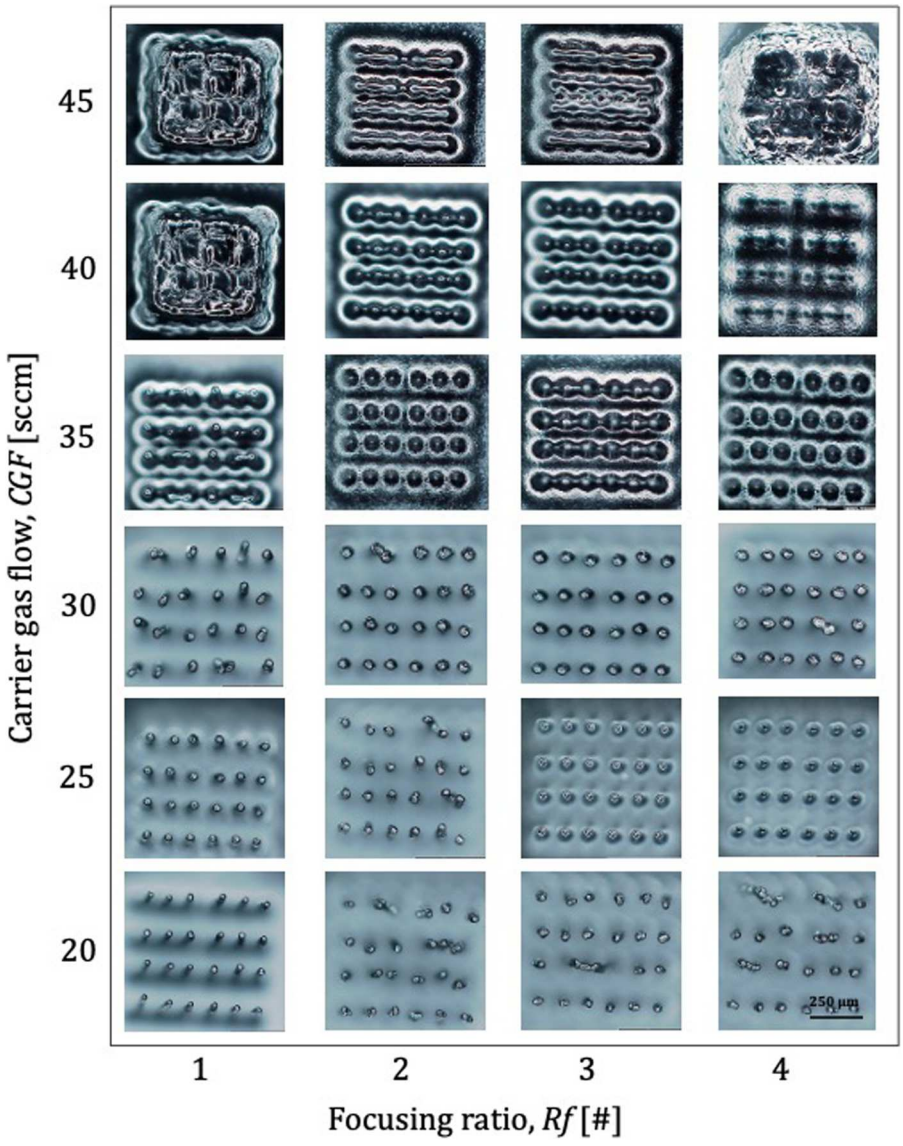

Figure 4. 3D AJ®P of PEDOT:PSS-based ink: representative top view images of micropillar arrays (6 × 4) for each combination of *Rf* = (1, 2, 3, 4) and *CGF* = (20, 25, 30, 35, 40, 45) sccm analysed (N = 3). Raw data from [22].

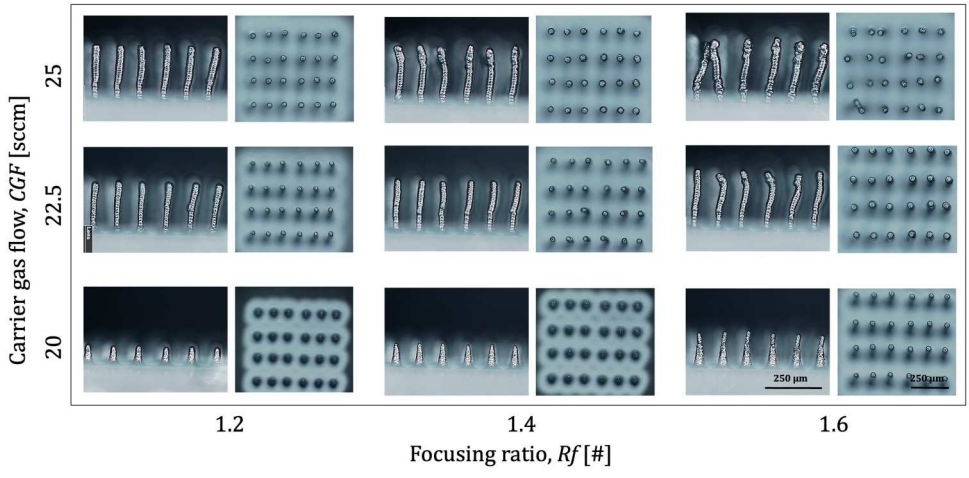

Figure 5. 3D AJ®P of PEDOT:PSS-based ink: representative lateral and top view images of micropillar arrays (6 × 4) for each combination of *Rf* = (1.2, 1.4, 1.6) and *CGF* = (20, 22.5, 25) analysed (N = 3). Raw data from [22].

Table 3. Cross-validated predictive performance metrics for all models across 2D and 3D geometries. Values represent the mean and standard deviation ($\mu \pm \sigma$) calculated from the outer folds of the nested cross-validation procedure.

Geometry	Model	RMSE	MAE	R^2
2D Line	RF	0.080 ± 0.020	0.060 ± 0.015	0.85 ± 0.08
	GPR	0.050 ± 0.010	0.040 ± 0.010	0.95 ± 0.05
	SVM	0.055 ± 0.010	0.045 ± 0.008	0.92 ± 0.06
	GAM	0.140 ± 0.030	0.100 ± 0.020	0.45 ± 0.15
	NN	0.115 ± 0.040	0.090 ± 0.025	0.68 ± 0.12
	STACK	0.070 ± 0.015	0.050 ± 0.010	0.90 ± 0.07
3D Micropillar	RF	0.030 ± 0.005	0.025 ± 0.003	0.65 ± 0.10
	GPR	0.025 ± 0.004	0.022 ± 0.002	0.68 ± 0.12
	SVM	0.030 ± 0.005	0.025 ± 0.003	0.65 ± 0.10
	GAM	0.028 ± 0.008	0.026 ± 0.003	0.50 ± 0.15
	NN	0.070 ± 0.035	0.028 ± 0.005	0.05 ± 0.20
	STACK	0.050 ± 0.015	0.038 ± 0.010	0.10 ± 0.10

Mean Absolute Error (MAE), and the coefficient of determination (R^2). These metrics were calculated separately for the 2D line and 3D micropillar datasets. All models were trained using the augmented dataset, which incorporated domain knowledge through the inclusion of physics motivated features (*e.g.* *TGF*, $\log R_f$) and constraints (*e.g.* InvalidFocus flags for $SGF < CGF$). The results, summarised in Table 3 and illustrated in Figure 6, demonstrate distinct performance trends across geometries and model types. For the 2D line geometry, several models achieved high predictive performance. GPR was the most accurate, yielding the highest average R^2 value of 0.95 ± 0.05, the lowest RMSE of 0.050 ± 0.010, and MAE of 0.040 ± 0.010 as illustrated in Figure 6(a, b and c), respectively. SVM, NN, RF and the stacked ensemble also performed well, attaining R^2 values above 0.80. The stack ensemble and GAM were the least performant models for this geometry. For the 3D micropillar geometry a general decline in predictive performance, as measured by R^2, was observed across all models. GPR, RF, and SVM were the most effective models, with nearly identical R^2 values of ~0.7. The RF and GAM models showed moderate performance,

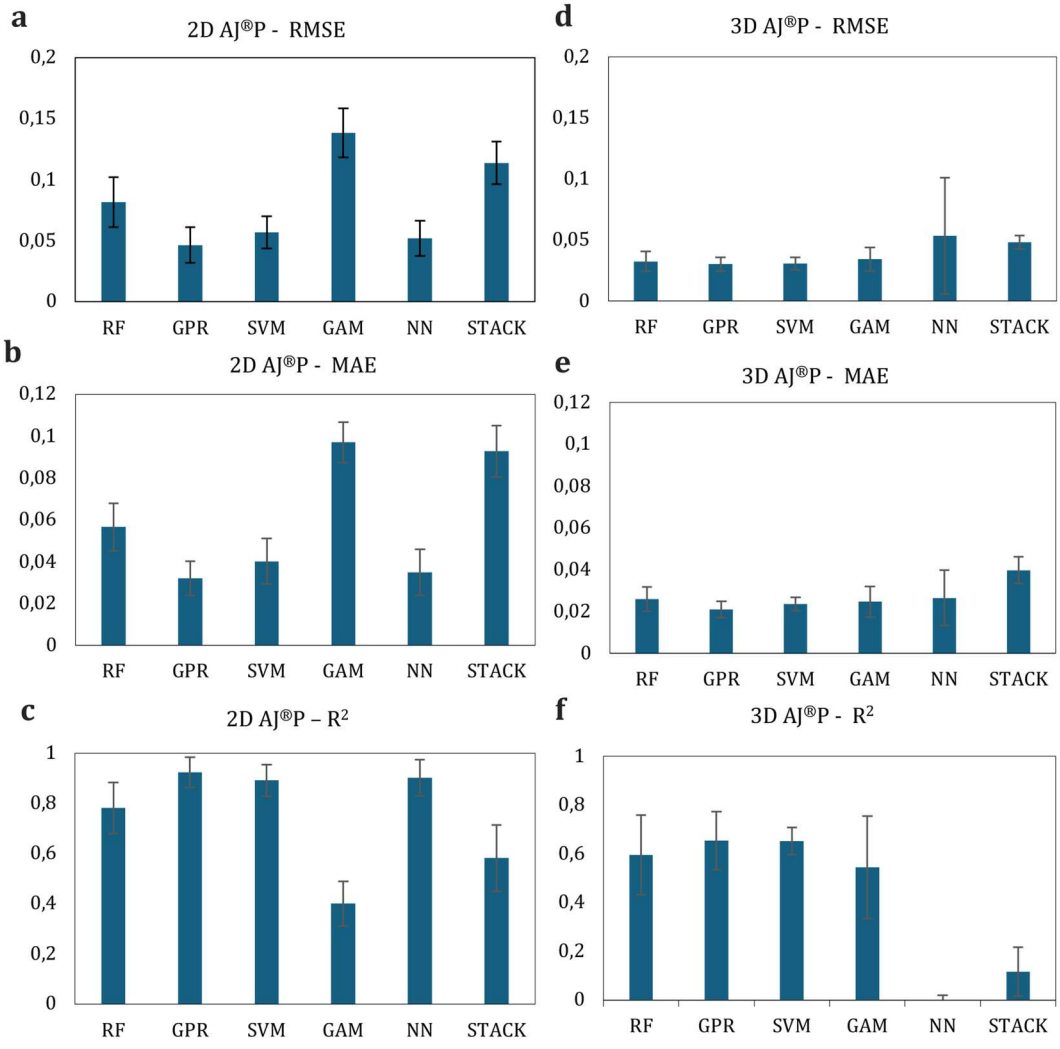

Figure 6. Cross-validated predictive performance metrics for all models across 2D and 3D geometries: values for 2D AJP as (a) RMSE, (b) MAE, (c) R^2, and for 3D AJP as (d) RMSE, (e) MAE, and (f) R^2.

while in this more challenging geometry setting, the performance of the stack ensemble and NN collapsed entirely. A key distinction emerges when comparing error magnitudes across geometries. Although the 3D models exhibit lower R^2 values, their RMSE and MAE values are generally smaller than those for the 2D models (Figure 6(d–f)).

This observation is directly related to the statistical distribution of the underlying data. The 2D dataset spans a wide quality range ($q^*_{2D} \in [0,\ 1]$ with mean(q^*_{2D}) = 0.66 and standard deviation σ = 0.39), for both high – and low-quality prints. In contrast, the 3D dataset is narrowly distributed within a higher-quality region ($q^*_{3D} \in [0.5,\ 1]$ with mean(q^*_{3D}) = 0.84 and σ = 0.14).

3.4. Feature importance and correlation analysis

To interpret the internal decision-making behaviour of the ML models and to quantify the contribution of individual input parameters, a feature importance analysis was conducted for both 2D and 3D geometries across all model architectures. Feature importance was computed using a permutation-based method, which evaluates significance of a feature by measuring the increase in prediction error, specifically, the change in RMSE, when the values of that feature are randomly shuffled. This process breaks relationship between the feature and output variable, revealing the degree of its predictive influence. The resulting normalised importance values are presented in Figure 7(a,b) for 2D line and 3D micropillars, respectively. To complement the model-based feature importance analysis and gain a more fundamental understanding of the linear relationships within the raw experimental data, a Pearson correlation analysis was performed. The Pearson correlation analysis is a statistical method that measures or first-order interactions between two variables by calculating a correlation coefficient (*r*) between -1 and 1, where 1 indicates a perfect positive linear correlation, -1 a perfect negative linear correlation, and 0 no linear correlation. The resulting correlation matrices for 2D and 3D AJP datasets are visualised as heatmaps in Figure 8.

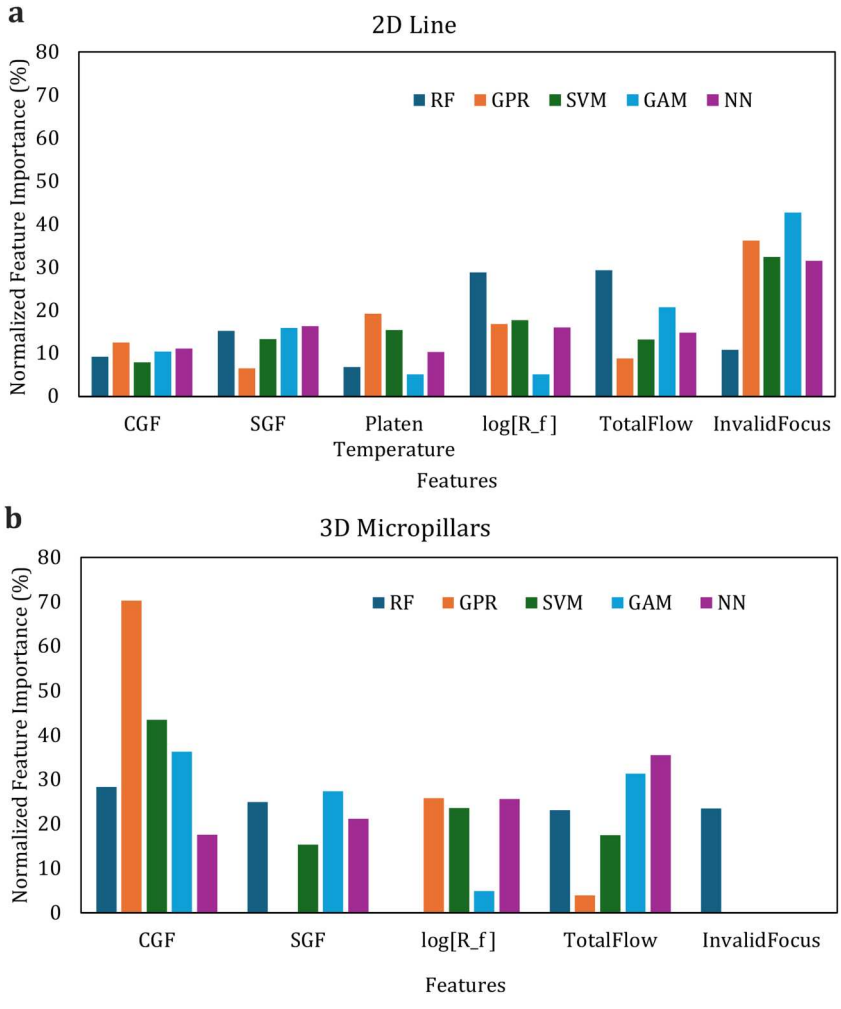

Figure 7. Normalised feature importance for: (a) 2D AJP line and (b) 3D AJP micropillars datasets, respectively.

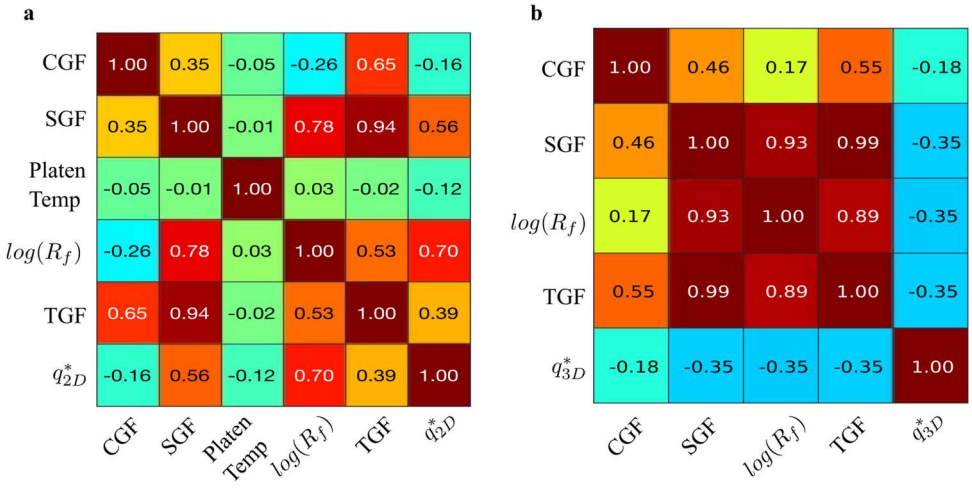

Figure 8. Pearson correlation heatmaps for key input and derived variables: (a) 2D AJP line dataset and (b) 3D AJP micropillar dataset.

3.5. Residual error analysis

To further examine model performance beyond aggregate metrics, a residual analysis was conducted. The residuals, calculated as the difference between the observed and predicted quality scores, offer a granular view of each model's error characteristics. By examining the distribution of these errors, we can diagnose systematic biases (*i.e.* a tendency to consistently over – or under-predict) and assess the stability and variance of the predictions. Violin plots were used to visualise these distributions for each model and geometry, combining the features of a box plot and a kernel density plot to show the probability density of the data at different values.

For the 2D line geometry, the residual distributions in Figure 9(a) reflect the broader range of quality scores present in the original dataset. The top-performing models, GPR, RF, and SVM, all exhibit residual distributions that are symmetric and centred around zero. In contrast, the GAM shows a significantly wider distribution with longer tails. The NN model exhibits the most problematic behaviour with its residual plot appearing as an extremely thin, long line, indicating a distribution with an exceptionally wide range of errors.

The analysis of the 3D micropillar geometry in in Figure 9(b) reveals much tighter residual distributions for most models. The GPR and RF models display the most compact and symmetric distributions, centred on zero. The SVM and GAM models show slightly unsymmetric distributions around zero. Most strikingly, the violin plot for the NN model again appears as a very long, thin line, with residuals extending far beyond those of any other model, providing definitive visual evidence of its failure to generalise for the 3D printing process.

3.6. Optimal parameter discovery

Optimal parameter values extracted by ML algorithms for both 2D and 3D AJP of PEDOT:PSS-based ink are summarised in Table 4. For 2D AJ printed lines, the various ML models employed led to consistent parameter

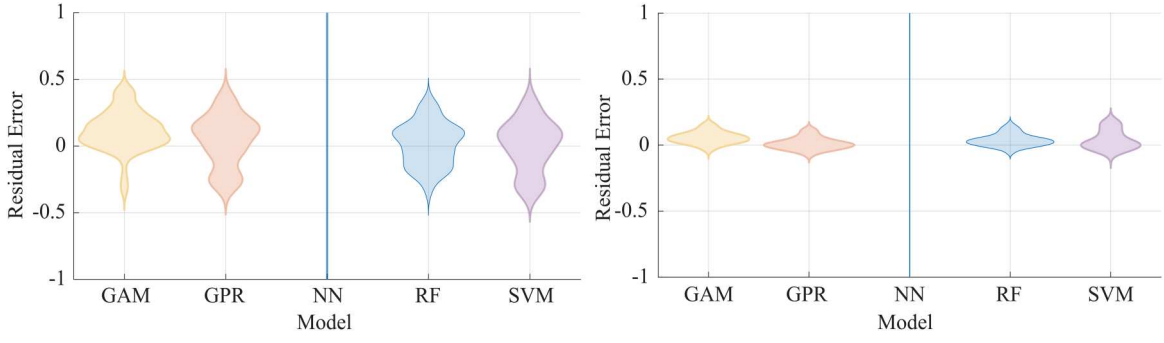

Figure 9. Distribution of residuals (Observed – Predicted Quality) for each model across 5-fold cross-validation for (a) 2D geometry and (b) 3D geometry. Each violin shows the spread of residuals for the corresponding model, indicating prediction accuracy and consistency.

Table 4. ML-derived optimal parameters for 2D and 3D AJP.

ML-derived optimal parameters for 2D AJP					
Mode	*Model*	*CGF [sccm]*	*SGF [sccm]*	*T [°C]*	*Rf [#]*
2D	RF	38.7	40.2	40	1.0
2D	GPR	30.5	51.1	25	1.7
2D	SVM	38.3	60.9	25	1.6
2D	GAM	38.9	40.8	43	1.0
2D	NN	35.4	77.5	25	2.2
ML-derived optimal parameters for 3D AJP					
Mode	*Model*	*CGF [sccm]*	*SGF [sccm]*	*T [°C]*	*Rf [#]*
3D	RF	27.4	27.5	80	1.0
3D	GPR	26.2	35.6	80	1.4
3D	SVM	26.4	26.6	80	1.0
3D	GAM	28.4	31.9	80	1.1
3D	NN	25.4	27.7	80	1.1

ranges. Specifically, across all algorithms, optimal *CGF* values fall between $30.5 \leq CGF \leq 38.9$ sccm, while *SGF* values range between $40.2 \leq SGF \leq 60.9$ sccm, with a *Rf* of $1.0 \leq Rf \leq 2.2$. The platform temperature for 2D printing was found to be optimal between 25°C and 40°C. In the case of 3D AJ printing for PEDOT:PSS micropillars, the consistency across ML models is even more pronounced. Optimal *CGF* values are narrowly distributed between $26.2 \leq CGF \leq 28.4$ sccm, with *SGF* ranging between $26.6 \leq SGF \leq 35.6$ sccm, and *Rf* values between $1.0 \leq Rf \leq 1.4$. The platform temperature was fixed at $T = 80$°C, as this corresponds to the experimental conditions used for training of the models.

4. Discussion

4.1. Experimental 2D and 3D AJP results

For 2D AJP, as expected, for all temperatures analysed, an increase in *Rf* leads to a decrease in LW, due to improved focusing of the aerosol stream. However, the trend for LW + OS does not always follow the same pattern. Deviations are observed at the extreme *CGF* values (20 and 50 sccm), likely due to instabilities in the printing process. These results suggest that optimal process parameters should be selected within the central range of the process window, where system stability is higher. Regarding the platen temperature, as previously reported, at $T = 25$ °C, the aerosol stream remains too wet to support stable thick-line formation. Conversely, at $T = 60$ °C, rapid solvent evaporation leads to significant line shrinkage and reduced process stability. At $T = 40$ °C, the behaviour is intermediate: solvent evaporation is sufficiently balanced to maintain both adequate material deposition and pattern definition, making this temperature preferable for achieving greater control over the printed features.

For 3D AJP, results demonstrate that both *CGF* and *Rf* play a critical role in determining the print quality and morphological stability of micropillars. High *CGF* values ($CGF \geq 35$ sccm) result in excessive material delivery, disrupting pillar formation, while low $CGF = 20$ sccm produces unstable structures with irregular tips. Optimal visual micropillar geometry is achieved within a narrow *CGF* range of 25–30 sccm, indicating the importance of balancing material flow and jet focus. Similarly, the *Rf* influences structural fidelity: $Rf = 1$ leads to well-defined, vertically aligned pillars, whereas increasing *Rf* to 3 introduces surface roughness and bending, likely due to instability in the aerosol stream.

These findings demonstrate the need for precise control of process parameters to maintain resolution and structural integrity in 3D AJP, and they establish a stable operating window.

4.2. ML algorithms

4.2.1. Model performance

As illustrated in Figure 6(a, b and c), the high predictive accuracy ($R^2 > 0.89$) achieved by the GPR, NN, and SVM models for the 2D line geometry demonstrates their ability in capturing the complex, non-linear process-property relationships inherent in AJP. The success of these diverse model architectures suggests that the underlying physics of single-layer deposition, while non-linear, are well-defined within the feature space and can be effectively learned by multiple advanced regression techniques.

The sharp decline in NN performance for the 3D geometry, from $R^2 = 0.68 \pm 0.12$ to $R^2 = 0.05 \pm 0.20$, requires careful examination. Although such a decline could suggest overfitting or architectural limitations, the learning curves presented in Supplementary Figure 1, demonstrate that this is not the case.

For the 3D dataset, training and validation losses decrease together and converge with a small and stable gap, which is a pattern indicative of successful model training rather than optimisation failure or overfitting. The observed reduction in R^2 is therefore not the result of poor learning but a statistical outcome of the data characteristics.

As defined by the relation $R^2 = 1 - \frac{MSE}{\sigma_{target}}$, its value is highly sensitive to the variance of the target variable (σ_{target}). The 3D dataset represents a highly constrained and narrow process window for successful fabrication, exhibits a significantly smaller quality score variance ($\sigma_{3D} \approx 0.14$) compared with the broader spread observed in the 2D dataset ($\sigma_{2D} \approx 0.39$). As a result, even the small absolute errors achieved by the NN, as indicated by its low RMSE and MAE values (Table 3), account for a large fraction of the total variance, mathematically

suppressing the R^2 value. This highlights a general challenge for machine learning in tightly constrained manufacturing processes. In such low-variance regimes, where with signal-to-noise is limited, flexible models such as NN may appear to underperform when evaluated solely by R^2 metrics, whereas more strongly regularised approaches such as Gaussian process regression and random forests tend to demonstrate more stable results.

A similar rationale explains the counter-intuitive performance collapse of the stacked ensemble, which, despite its strong performance on the 2D dataset, failed to generalise for the 3D case. The strength of stacked ensembles lies in the meta-learner's capacity to correct for diverse and complementary errors among the base models. However, in the constrained, low-variance environment of the 3D dataset, the top-performing base learners (GPR, RF, and SVM) produced highly similar predictions, leading to strongly collinear error patterns. Without sufficient diversity to exploit, the ridge-regression meta-learner, was unable to extract any additional information beyond what the best single model had already captured. Therefore, the apparent collapse of stack ensemble performance reflects the challenging statistical properties of the data rather than an inadequacy of the meta-learner itself.

4.2.2. Feature importance and correlation

The feature importance and correlation analyses provide critical insights into the governing physics of AJP for different geometries. For the 2D line dataset, as illustrated in Figure 7(a), the binary indicator *InvalidFocus* emerged as the most influential feature across four of the five models. This feature flags whether the process is operating outside a known stable range for the focusing ratio ($Rf < 1$), which is widely recognised to result in unstable jetting and poor print outcomes. The high importance of $\log(R_f)$ and *TGF* in the RF model, combined with the strong positive Pearson correlation ($r = 0.70$) between $\log(R_f)$ and print quality index, shown in Figure 8(a), reinforces the principle that a well-collimated, stable aerosol stream is crucial for producing well-defined 2D lines.

The significant shift in feature importance for the 3D geometry, illustrated in Figure 7(b), is a key finding of this work. The consistent identification of *CGF* as the most influential feature by the majority of models, especially its significantly high importance for the top-performing GPR model, indicates a fundamental change in the process dynamics. This suggests that for the layer-by-layer buildup of HAR structures, the precise control of the material deposition rate, which is directly governed by *CGF*, becomes more critical than the jet focusing itself. Any inconsistency in material delivery can lead to cumulative errors that compromise the structural integrity of the pillar as it grows in height. This interpretation is strongly supported by the reversal of the Pearson correlation for $\log(R_f)$ from strongly positive in the 2D case to negative in the 3D case ($r = -0.35$), presented in Figure 8(b). This hints that for 3D HAR micropillar fabrication, simply increasing the *Rf* is detrimental and suggests that 3D printing operates within a much narrower and more sensitive process window where stability is achieved. This analysis underscores why simple linear models are insufficient for process optimisation, particularly for the 3D case, and reinforces the necessity of employing sophisticated, non-linear ML models to capture these complex process dynamics.

4.2.3. Residual errors

The residual analysis offers a powerful visual confirmation of the model performance hierarchy and is crucial for assessing model reliability. As shown in Figure 9(a and b), the residual distributions for both GPR and RF models exhibit a symmetric shape centred around zero for both 2D and 3D geometries, respectively. This pattern suggests that the predictions made by these models are, on average, unbiased. Such behaviour reinforces their suitability as stable surrogate models. In contrast, the NN model displays clear signs of instability. Despite achieving a high R^2 of 0.90 for 2D AJP, its residual plot reveals its unreliability by showing a wide error distribution. This indicates that the NN model is prone to produce large, unpredictable errors. This could be explained by the reliance of NNs on large datasets for training. This instability of NN model, despite its high aggregate performance in 2D case, underscores the importance of not relying on a single performance metric but rather using a holistic evaluation that includes error analysis to ensure model robustness. In summary, the residual analysis provides a qualitative and quantitative confirmation of the model performance hierarchy. It demonstrates that the GPR and RF models are not only the most accurate but also the most stable and unbiased predictors for both 2D and 3D AJP quality.

4.3. Optimal parameters

The integration of ML algorithms with experimental validation has provided robust insights into the optimal process parameters for AJP of PEDOT:PSS in both 2D and 3D configurations. The ML models, including RF, GPR, SVM, GAM, and NN, identified parameter sets that show strong alignment with experimental outcomes, confirming the utility of data-driven optimisation in

fine-tuning AJP processes. For 2D printing, the optimal *CGF* values predicted by the models range between $30.5 \leq CGF \leq 38.9$ sccm, $40.2\ 2 \leq SGF \leq 77.5$ sccm, and $1.04\ 2 \leq Rf \leq 2.19$, with platform temperatures predominantly at 25–40 °C. These results reflect a relatively broad and flexible process window. Experimental validation showed that combinations such as $Rf = 2$, $CGF = 40$ sccm, and $T = 40$ °C consistently produced high-quality printed lines with reduced OS and well-defined features (Figure 2). The trend clearly suggests that higher *Rf* values improve resolution, while higher *CGF* values increase line width but risk OS if not balanced by proper *Rf* and *SGF*. Notably, while models like NN predicted high *SGF* (77.5 sccm) and *Rf* (2.19), these values may offer more theoretical optimisation under noise-tolerant conditions but are harder to manage experimentally due to jet instability. The overall agreement across models suggests that 2D AJP is more tolerant to parameter variations, as long as aerosol focus and deposition balance are maintained. It is also evident that higher platen temperatures, such as $T = 40$ °C, reduce the need for highly focused *SGF*, as accelerated solvent evaporation enhances ink deposition control. In contrast, at lower platen temperatures (*e.g.* $T = 25$ °C), ML models predict either reduced *CGF* or significantly higher *SGF* values, such as 51.1, 60.9, or even 77.5 sccm, to maintain jet focus and compensate for slower solvent evaporation. This reflects a temperature-dependent shift in the balance between gas flows required to stabilise the aerosol stream.

In contrast, the ML-predicted optimal ranges for 3D AJP are considerably narrower, reflecting heightened process sensitivity that is critical for maintaining structural integrity. This observation was formally quantified through a bootstrap resampling analysis ($n = 1000$ for 2D and $n = 500$ for 3D), which estimated 95% confidence intervals (CIs) for the optimal carrier gas flow (*CGF*) using the top-performing GPR model. The results, presented in Supplementary Figure 2, highlights a clear difference in process latitude. For 2D printing, the optimal *CGF* spans a broad window of 30–40 sccm, with a 95% CI width of approximately 8–10 sccm. In contrast, the 3D micropillar process is highly constrained, with the optimal *CGF* centred at 25–27 sccm and a 95% CI width of only about 2 sccm. This greater than four-fold difference provides robust quantitative evidence that 3D AJP is significantly more sensitive to parameter variations therefore requires substantially tighter process control to ensure high-quality, reproducible outcomes. Experimental results confirm this observation. Deviations from the narrow optimal range, particularly $CGF \geq 30$ sccm or $Rf > 1.4$, resulted in merged or unstable micropillars, as shown in Figure 3 and Figure 4.

The close agreement among all five ML models further reinforces the reliability of these predictions and points to a stable, reproducible parameter window for volumetric feature fabrication. Together, these findings suggest that while 2D AJP allows for more flexibility in parameter tuning, 3D AJP benefits from tight process control and narrow parameter bounds. ML tools proved effective in identifying these regions, streamlining experimental efforts and reducing trial-and-error cycles. The consistency between model predictions and experimental outcomes supports the feasibility of closed-loop optimisation for AJP systems, enabling smarter, more efficient manufacturing workflows for high-resolution conductive polymer structures.

5. Conclusions and future perspectives

This study presents a robust, physics-informed ML framework capable of predicting and optimising the print quality of both 2D lines and 3D HAR micropillars in the AJP process. By addressing the inherent challenges of non-linear, geometry-dependent process dynamics and experimental data amount, the proposed methodology offers insights in the AJP process understanding and optimisation. The framework demonstrated high predictive accuracy for 2D geometries, with models such as GPR and SVM achieving R^2 values exceeding ≈ 0.90. For the more complex 3D structures, GPR and SVM also maintained respectable performance ($R^2 \approx 0.65$), underscoring the importance of model selection based on task complexity and data availability. Importantly, this work quantitatively highlights that jet collimation primarily governs 2D line quality, while the carrier gas flow critically influences 3D HAR pillar formation. The validated surrogate models enable efficient identification of optimal process windows, confirming that 3D AJP has narrower tolerances and tighter control than 2D AJP. The study also introduces a comprehensive model evaluation protocol, demonstrating that conventional accuracy metrics must be supplemented with stability and interpretability analyses to ensure model reliability.

Future research will extend this framework toward multi-objective optimisation by incorporating functional performance metrics such as electrical conductivity and mechanical strength, while also exploring transfer learning strategies to accelerate model development for new materials and geometries. A longer-term vision is the integration of these models with digital twins to support closed-loop control systems for autonomous process optimisation.

The proposed pathway relies on a hybrid, two-stage control architecture, designed to balance predictive accuracy with operational responsiveness. The initial stage would involve an offline optimisation using the high-fidelity surrogate models validated in this study. These models would identify a robust, near-optimal set of starting parameters, subject to known process constraints (e.g. $SGF \geq CGF$) and actuator limits.

The second stage would operate during the printing process through a computationally efficient, online adaptive controller. This low complexity adaptive controller would make real-time adjustments to account for process drift and stochastic variations. Implementation of this stage would require integration with an in-situ monitoring system, such as image-based analysis of linewidth or optical scattering measurements of the aerosol stream, to provide the continuous quality feedback necessary for closed-loop operation. Based on this feedback, a low-complexity adaptive control algorithm would propose incremental adjustments to critical parameters. To ensure process stability and purposeful intervention, an adjustment would be implemented only when two conditions are satisfied. First, the candidate parameters must remain within predefined operational bounds defined by process constraints and actuator limits to maintain reliable operation. Second, the surrogate model must predict an improvement in output quality that exceeds a specified threshold. This threshold functions as a practical significance criterion that suppresses unnecessary interventions, avoids chasing minor fluctuations, and limits the risk of variance amplification in otherwise stable operation. The frequency of this control loop would be governed by the sensing and computation latencies, which in typical laboratory settings can support updates on the order of seconds.

By combining surrogate-driven global optimisation with adaptive real-time control, this framework establishes a pathway toward self-correcting, zero-defect manufacturing. In addition to advancing technical precision, it offers broader impact by reducing waste and energy use, accelerating innovation cycles, and supporting distributed, scalable production. Such capabilities position additive manufacturing at the forefront of smart, sustainable, and autonomous manufacturing ecosystems.

Acknowledgements

The authors acknowledge MICS (Made in Italy – Circular and Sustainable) Extended Partnership (Next Generation EU (Italian PNRR – M4 C2, 1.3–D.D.1551.11-10-2022, PE00000004 CUP D73C22001250001)). The authors acknowledge the Advanced Manufacturing Laboratory (AML) at KU Leuven for the use of the AJP system. CRediT: M. Sharma: Conceptualisation, Data curation, Formal analysis, Software, Investigation, Methodology, Validation, Visualisation, Writing – original draft; M. Seiti: Conceptualisation, Formal analysis, Funding acquisition, Resources, Project administration, Supervision, Methodology, Validation, Writing, review & editing.

Author contributions

CRediT: **Mohit Sharma:** Data curation, Investigation, Methodology, Resources, Software, Validation, Visualization, Writing – original draft; **Miriam Seiti:** Conceptualization, Formal analysis, Investigation, Methodology, Project administration, Resources, Supervision, Visualization, Writing – review & editing.

Disclosure statement

No potential conflict of interest was reported by the author(s).

Funding

This work was supported by Next Generation EU (Italian PNRR – M4 C2, 1.3–D.D.1551.11-10-2022, PE00000004 CUP D73C22001250001).

Data availability statement and deposition

The datasets generated and analysed during this study are openly available at https://github.com/mohit-nith/AJP_Printability_ML, under the assigned persistent identifier. All data are shared under a Creative Commons Attribution 4.0 International (CC BY 4.0) license. This comprehensive dataset includes all materials necessary to reproduce the findings presented in the manuscript:

- The complete experimental dataset for both 2D line and 3D micropillar geometries, including raw process parameters (carrier gas flow, sheath gas flow, and platen temperature) alongside the corresponding normalised quality scores.
- A full table of cross-validated performance metrics – RMSE, MAE, and R^2 – reported with mean and standard deviation values for each machine learning model.

Generative AI Disclosure

This manuscript was prepared with the assistance of the generative AI tool ChatGPT (version GPT-4) for rephrasing certain sentences to improve English readability. The tool was used only to enhance language clarity and did not contribute to the scientific content or interpretation of the results.

ORCID

Mohit Sharma http://orcid.org/0000-0001-6310-2416
Miriam Seiti http://orcid.org/0000-0002-9619-3788

References

[1] Suganuma K. *Introduction to printed electronics*. New York: SpringerLink; 2014.

[2] Park Y-G, Insik Y, Chung WG, et al. High-Resolution 3D printing for electronics. Adv Sci. 2022;9:2104623. doi:10.1002/advs.202104623

[3] Tay RY, Song Y, Yao DR, et al. Direct-ink-writing 3D-printed bioelectronics. Mater Today. 2023;71:135–151. doi:10.1016/j.mattod.2023.09.006

[4] Zavanelli N, Yeo W-H. Advances in screen printing of conductive nanomaterials for stretchable electronics. ACS Omega. 2021;6:9344–9351. doi:10.1021/acsomega.1c00638

[5] Søndergaard RR, Hösel M, Krebs FC. Roll-to-roll fabrication of large area functional organic materials. J Polym Sci Part B: Polym Phys. 2013;51(1):16–34. doi:10.1002/polb.23192

[6] Cummins G, Desmulliez MPY. Inkjet printing of conductive materials: a review. Circuit World. 2012;38:193–213. doi:10.1108/03056121211280413

[7] Wilkinson NJ, Smith MAA, Kay RW, et al. A review of aerosol jet printing—a non-traditional hybrid process for micro-manufacturing. Int J Adv Manuf Technol. 2019;105:4599–4619. doi:10.1007/s00170-019-03438-2

[8] Seiti M, Degryse O, Monica Ferraro R, et al. 3D Aerosol Jet® printing for microstructuring: Advantages and Limitations. Int J Bioprinting. 2023;9:57–74. doi:10.36922/ijb.0257

[9] Giuri A, Striani R, Carallo S, et al. Waste carbon ashes/PEDOT: PSS nano-inks for printing of supercapacitors. Electrochim Acta. 2023;441:141780. doi:10.1016/j.electacta.2022.141780

[10] Seiti M, Ginestra PS, Ferraris E. Aerosol Jet Printing of 3D biocompatible gold nanoparticle-based micro-structures. In: Carrino L, Galantucci LM, Settineri L, editors. *Selected topics in manufacturing: emerging trends from the perspective of AITeM's young researchers*. Cham: Springer Nature Switzerland; 2024. p. 19–34.

[11] Salary RR, Lombardi JP, Weerawarne DL, et al. A State-of-the-art review on aerosol jet printing (AJP) additive manufacturing process. Am Soc Mech Eng Digital Collect. 2019;1:3008–3024.

[12] Seiti M, Verma A, Degryse O, et al. Chapter 4 - aerosol jet-based printing for smart multifunctional nano-inks. In: Gupta RK, Nguyen TA, editors. *Smart multifunctional nano-inks*. Amsterdam, Netherlands: Elsevier; 2023. p. 75–90.

[13] Jahan S, Hu C, Yuan B, et al. Aerosol jet 3D printing of gold micropillars and their behavior under compressive loads. Addit Manuf. 2024;92:104385.

[14] Smith BN, Ballentine P, Doherty JL, et al. Aerosol Jet Printing Conductive 3D Microstructures from Graphene Without Post-Processing. Small. 2024;20:2305170. doi:10.1002/smll.202305170

[15] Hines DR, Gu Y, Martin AA, et al. Considerations of aerosol-jet printing for the fabrication of printed hybrid electronic circuits. Addit Manuf. 2021;47:102325.

[16] Fuhr G, Shirley SG. Biological Application of Microstructures. In: Manz A, Becker H, editors. *Microsystem technology in chemistry and life science*. Berlin: Springer; 1998. p. 83–116.

[17] Wei M, Zhou Q, Ma X, et al. Review of biomimetic ordered microstructures in advancing synergistic integration of adhesion and microfluidics. RSC Adv. 2024;14:11643–11658. doi:10.1039/D3RA07698A

[18] Ali MA, Fei Zhang G, Hu C, et al. An Advanced Healthcare Sensing Platform for Direct Detection of Viral Proteins in Seconds at Femtomolar Concentrations via Aerosol Jet 3D-Printed Nano and Biomaterials. Adv Mater Interfaces. 2024;11:2400005. doi:10.1002/admi.202400005

[19] Lopez-Hallman R, Rodriguez R, Lai Y-T, et al. All-solid-state battery fabricated by 3D aerosol jet printing. Adv Eng Mater. 2024;26:2300953. doi:10.1002/adem.202300953

[20] Hu C, Jahan S, Yuan B, et al. 3D-AJP: fabrication of advanced microarchitected multimaterial ceramic structures via binder-free and auxiliary-free aerosol jet 3D nanoprinting. Adv. Sci. 2025;12:2405334. doi:10.1002/advs.202405334

[21] Seiti M, Degryse O, Ferraris E. Aerosol. Aerosol Jet® printing 3D capabilities for metal and polymeric inks. Mater Today Proc, 2022;70:38–44. https://doi.org/10.1016/j.matpr.2022.08.488

[22] Ceretti E, Sharma M, Ferraris E, et al. Printability assessment and modelling for process optimization of 3D Aerosol Jet® printed high aspect ratio microstructures. CIRP Ann. 2025;74(1):287–291.

[23] Li M, Yin S, Liu Z, et al. Machine learning enables electrical resistivity modeling of printed lines in aerosol jet 3D printing. Sci Rep. 2024;14:14614. doi:10.1038/s41598-024-65693-y

[24] Liu Y, Yin S, Liu Z, et al. A machine learning framework for process optimization in aerosol jet 3D printing. Flex Print Electron. 2023;8:025017. doi:10.1088/2058-8585/acd794

[25] Seiti M, Ginestra PS, Ferraro RM, et al. Aerosol jet® printing of poly (3, 4-Ethylenedioxythiophene): Poly (Styrenesulfonate) onto micropatterned substrates for neural cells in vitro stimulation. Int J Bioprinting. 2022;8:50–65. doi:10.18063/ijb.v8i1.504

[26] Yang Y, Deng H, Fu Q. Recent progress on PEDOT:PSS based polymer blends and composites for flexible electronics and thermoelectric devices. Mater Chem Front. 2020;4:3130–3152. doi:10.1039/D0QM00308E

[27] Mahajan A, Frisbie CD, Francis LF. Optimization of Aerosol Jet Printing for High-Resolution,: High-Aspect Ratio Silver Lines. ACS Appl Mater Interfaces. 2013;5:4856–4864. doi:10.1021/am400606y

[28] Dalal N, Gu Y, Chen G, et al. Effect of gas flow rates on quality of aerosol jet printed traces with nanoparticle conducting ink. J Electron Packag. 2019;142:011012–011023.

[29] Ramesh S, Mahajan C, Gerdes S, et al. Numerical and experimental investigation of aerosol jet printing. Addit Manuf. 2022;59:103090.

[30] Li G, Wang S, Zhang Z, et al. precision control of aerosol jet printing for conformal electronics fabrication with ultra-fine and wide-range resolution. Adv Mater Technol. 2025;10:2402114. doi:10.1002/admt.202402114

[31] Meng L, McWilliams B, Jarosinski W, et al. Machine learning in additive manufacturing: a review. JOM. 2020;72:2363–2377. doi:10.1007/s11837-020-04155-y

[32] Frazier PI. Bayesian optimization in recent advances in optimization and modeling of contemporary problems 255–278 (INFORMS, 2018).
[33] Torgo L, Ribeiro RP, Pfahringer B, et al. SMOTE for Regression. In: Correia L, Reis LP, Cascalho J, editors. *Progress in artificial intelligence*. Berlin: Springer; 2013. p. 378–389.
[34] Chawla NV, Bowyer KW, Hall LO, et al. SMOTE: synthetic minority over-sampling technique. J Artif Intell Res. 2002;16:321–357. doi:10.1613/jair.953
[35] Branco P, Torgo L, Ribeiro RP. Smogn: a pre-processing approach for imbalanced regression. In Proceedings of the First International Workshop on Learning with Imbalanced Domains: Theory and Applications 36–50 (PMLR, 2017).
[36] Breiman L. Random Forests. Mach Learn. 2001;45:5–32. doi:10.1023/A:1010933404324
[37] Biau G, Scornet E. A random forest guided tour. Test. 2016;25:197–227. doi:10.1007/s11749-016-0481-7
[38] Rasmussen CE, Williams CKI. *Gaussian processes for machine learning*. Cambridge, Massachusetts: The MIT Press; 2005.
[39] Akbari P, Zamani M, Mostafaei A. Machine learning prediction of mechanical properties in metal additive manufacturing. Addit Manuf. 2024;91(5):104320.
[40] Drucker H, Burges C, Kaufman L, et al. Support vector regression machines. Adv Neural Inf Process Syst. 1997;28:779–784.
[41] Smola AJ, Schölkopf B. A tutorial on support vector regression. Stat Comput. 2004;14:199–222. doi:10.1023/B:STCO.0000035301.49549.88
[42] *Statistical Models in S*. New York: Routledge, 2017.
[43] Marx BD, Eilers PHC. Direct generalized additive modeling with penalized likelihood. Comput Stat Data Anal. 1998;28:193–209. doi:10.1016/S0167-9473(98)00033-4
[44] Hornik K. Approximation capabilities of multilayer feedforward networks. Neural Netw. 1991;4:251–257. doi:10.1016/0893-6080(91)90009-T
[45] Powell D, Magnanini MC, Colledani M, et al. Advancing zero defect manufacturing: a state-of-the-art perspective and future research directions. Comput Ind 2022;136:103596. doi:10.1016/j.compind.2021.103596
[46] Pike JA, Klett J, Kunc V, et al. Machine learning in additive manufacturing: a review of learning techniques and tasks, 2022.
[47] Tafoya RR, Secor EB. Understanding and mitigating process drift in aerosol jet printing. Flex Print Electron. 2020;5:015009. doi:10.1088/2058-8585/ab6e74